PCCP

PAPER

View Article Online
View Journal | View Issue

Cite this: *Phys. Chem. Chem. Phys.*, 2024, **26**, 22049

Full optimization of dynamic nuclear polarization on a 1 tesla benchtop polarizer with hyperpolarizing solids†‡

Ewoud Vaneeckhaute,*[a] Charlotte Bocquelet,[a] Léa Bellier,[a] Huu-Nghia Le,[b] Nathan Rougier,[a] Shebha Anandhi Jegadeesan,[c] Sanjay Vinod-Kumar,[c] Guinevere Mathies,[c] Laurent Veyre,[b] Chloe Thieuleux,[b] Roberto Melzi,[d] Daniel Banks,[e] James Kempf,[e] Quentin Stern[a] and Sami Jannin[a]

Hyperpolarization by dissolution dynamic nuclear polarization (dDNP) provides the opportunity to dramatically increase the weak nuclear magnetic resonance (NMR) signal of liquid molecular targets using the high polarization of electron radicals. Unfortunately, the solution-state hyperpolarization can only be accessed once since freezing and melting of the hyperpolarized sample happen in an irreversible fashion. A way to expand the application horizon of dDNP can therefore be to find a recyclable DNP alternative. To pursue this ambitious goal, we recently introduced the concept of recyclable hyperpolarized flow (HypFlow) DNP where hyperpolarization happens in porous hyperpolarizing solids placed in a compact benchtop DNP polarizer at a magnetic field of 1 T and a temperature of 77 K. Here we aim to optimize the radical concentrations immobilized in hyperpolarizing solids with the objective of generating as much polarization as possible in a timeframe (<1 s) compatible with future recyclable DNP applications. To do so, the solid-state DNP enhancement factors, build-up rates and DNP spectra of different hyperpolarizing solids containing various nitroxide radical loadings (20–74 μmol cm^{-3}) are compared against the DNP performance of varying nitroxide concentrations (10–100 mM) solvated in a glassy frozen solution. We demonstrate that in <1 s, polarization enhancement goes up to 56 and 102 with surface-bound and solvated radicals, respectively, under the optimized conditions. For the range of nitroxide concentrations used cross effect DNP seems to be the dominant mechanism under benchtop conditions. This was deduced from the electron paramagnetic resonance (EPR) lineshape of TEMPOL investigated using Q-band EPR measurements.

Received 15th May 2024,
Accepted 10th July 2024

DOI: 10.1039/d4cp02022g

rsc.li/pccp

1. Introduction

Nuclear magnetic resonance (NMR) is an indispensable spectroscopic tool for the analysis of complex analyte mixtures.[1–3] Liquid-state NMR excels in providing structurally rich spectroscopic output that is robust, reliable, and reproducible due to the non-destructive properties of the technology. Moreover, the sensitivity constraints that are traditionally limiting NMR applications can be circumvented by recent advancements in hyperpolarization strategies temporarily bringing molecular targets into a transient hyperpolarized – or signal-enhanced – state.[4–6]

Dissolution dynamic nuclear polarization (dDNP) is uniquely fitted for providing the higher sensitivity required for advancing mixture analysis applications *via* liquid-state NMR.[7–9] Using dDNP, any analyte brought in close contact (1–5 nm) with a neighbouring paramagnetic radical with highly spin-polarized electrons in a frozen (1–4 K), glassy state can become transiently fuelled with nuclear spin hyperpolarization through microwave (μw) assisted polarization transfer inside a magnetic field.[10] Then, spin diffusion, that thrives on energy-conservative dipolar flip-flops, allows for spontaneous redistribution of nuclear polarization to any analyte target (Fig. 1a).[11] Afterwards, rapid dissolution with hot pressurized

[a] *Université Claude Bernard Lyon 1, CNRS, ENS Lyon, UCBL, CRMN UMR 5082, 69100 Villeurbanne, France. E-mail: ewoud.vaneeckhaute@univ-lyon1.fr*
[b] *Université Claude Bernard Lyon 1, Institut de Chimie de Lyon, CP2M UMR 5128 CNRS-UCBL-CPE Lyon, 69616 Villeurbanne, France*
[c] *Department of Chemistry, University of Konstanz, Universitätsstr. 10, 78464, Konstanz, Germany*
[d] *Bruker Italia S.r.l., Viale V. Lancetti 43, 20158 Milano, Italy*
[e] *Bruker Biospin, Billerica, Massachusetts 01821, USA*

† Raw data and MATLAB codes are available in the Zenodo repository **https://doi.org/10.5281/zenodo.11120018**.

‡ Electronic supplementary information (ESI) available: Additional NMR and DNP results and HYPSO-5 material properties. See DOI: **https://doi.org/10.1039/d4cp02022g**

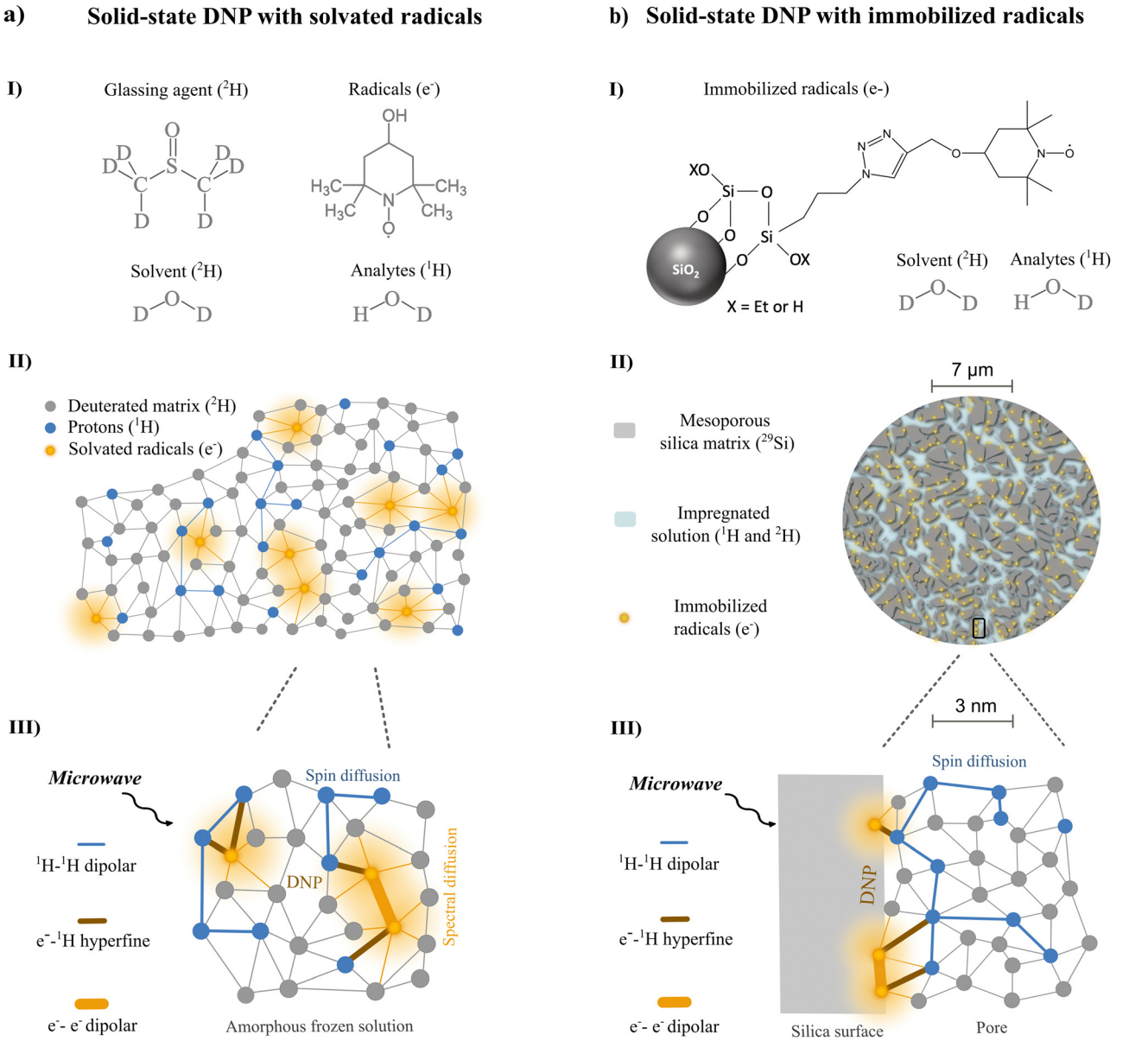

Fig. 1 Overview of solid-state dynamic nuclear polarization (DNP) principles to hyperpolarize analytes using paramagnetic radicals (a) randomly distributed in an amorphous frozen solution or (b) immobilized on the surface of a porous material when placed inside a magnetic field and cryogenic temperatures. In (I) the Lewis structure of the chemical components required for DNP with solvated radicals or hyperpolarizing solids are highlighted. In (II) a graphical representation of the radical and analyte distribution is provided in both cases. In (III) the principle of transferring spin hyperpolarization from spin polarized electrons (orange) to neighbouring nuclear spins (blue) embedded in most commonly a deuterated matrix (grey) is presented.

water melts and transfers the sample for hyperpolarized liquid-state NMR detection where fine structural features (Hz) of the analytes are revealed, previously obscured by strong dipolar interactions (kHz) in the frozen state.[12] The general applicability of bringing analytes in close contact with a polarizing agent explains why sensitivity enhancement by dDNP is exceptionally promising towards hyperpolarization of multi-component chemical mixtures.[13,14]

However, the presence of the paramagnetic polarizing agents for fuelling hyperpolarization in the frozen state, also induces detrimental hyperpolarization losses both during and after the phase transition when in intricate contact with the analytes.[15] As hyperpolarized analytes are forced into an out-of-equilibrium magnetic state, paramagnetic relaxation caused by the close presence of unpaired electrons drastically reduces the longitudinal relaxation time of the nuclear spins. This is caused by stochastic fluctuations of the electron spin state that are similar in frequency to the nuclear Larmor frequency. In solids, the main source of these fluctuations are spontaneous electron-pair flip-flops or electron longitudinal relaxation processes, while in liquids, the main source is considered molecular translational diffusion.[16–18] Yet in all cases, the presence of

electrons acts as a strong hyperpolarization sink. Consequentially, within milliseconds in solids and seconds in liquids, hyperpolarization after the phase transition is mostly lost. Therefore, after transferring the paramagnetic hyperpolarized mixture into a dedicated liquid-state NMR detection unit, only a limited one-shot window exists in which structural analysis of complex mixtures can be performed. This is considered an important bottleneck in applying dDNP for hyperpolarized NMR.[19,20]

Hyperpolarizing solids offer an elegant way to circumvent this roadblock. They are composed of porous materials (*e.g.* silica- or polymer-based) containing covalently immobilized radicals in which the analytes of interest can be impregnated (Fig. 1b).[21–23] There is additional control over the physical distance between the unpaired electrons, distributed along the silica pore channels or even embedded in the solid framework, and the impregnated analytes residing in the pores.[24] Since the rate of direct paramagnetic induced relaxation is dependent on the inverse sixth power of the distance between the electron and nuclear spins,[10,11,25] optimization of pore geometry and radical immobilization can reduce the relaxation sink.[26,27] On top, the ability to physically extrude the hyperpolarized analytes after melting has even more opportunities: the production of pure analyte solutions not contaminated and affected by any paramagnetic species becomes suddenly feasible.[28,29]

We aim to reach a new horizon of DNP applications by establishing methods, equipment and chemical systems that enable a repeated sequence of DNP hyperpolarization and solution-state NMR observation. This approach takes advantage of hyperpolarizing solids which will be key to developing a recyclable DNP alternative without dilution nor radical contamination. To pursue this ambitious goal, we recently introduced the concept of recyclable hyperpolarized flow (HypFlow) DNP in Bocquelet *et al.*[30] The HypFlow DNP approach aims at operating with a closed loop cycle where hyperpolarization is generated in a heterogenous stationary phase of silica-based polarizing matrices (HYPSO) positioned in a compact and helium-free benchtop DNP polarizer which is schematically summarized in Fig. 2a and b. By utilizing a benchtop DNP polarizer at a magnetic field of 1 T and a temperature of 77 K, we gain a more modest sensitivity boost compared to traditional dDNP, but the higher temperature and accessible conditions also create the opportunity when hyperpolarizing matrices are used, to enable rapid melt and pure sample extraction in the future.[31,32] A single sample could therefore be hyperpolarized several times if a dilution-free melting step is envisioned.[33,34] When the sample is then pumped through a closed loop coupled to a benchtop NMR spectrometer for liquid-state detection, this could allow for compatibility with hyperpolarized two-dimensional NMR structural characterization advancing in-depth chemical mixture analysis.[35]

In this context, we present a general systematic DNP study for a series of different nitroxide radical concentrations solvated in a glassy frozen solution (Fig. 1a) and immobilized in hyperpolarizing solids (Fig. 1b) using the benchtop DNP

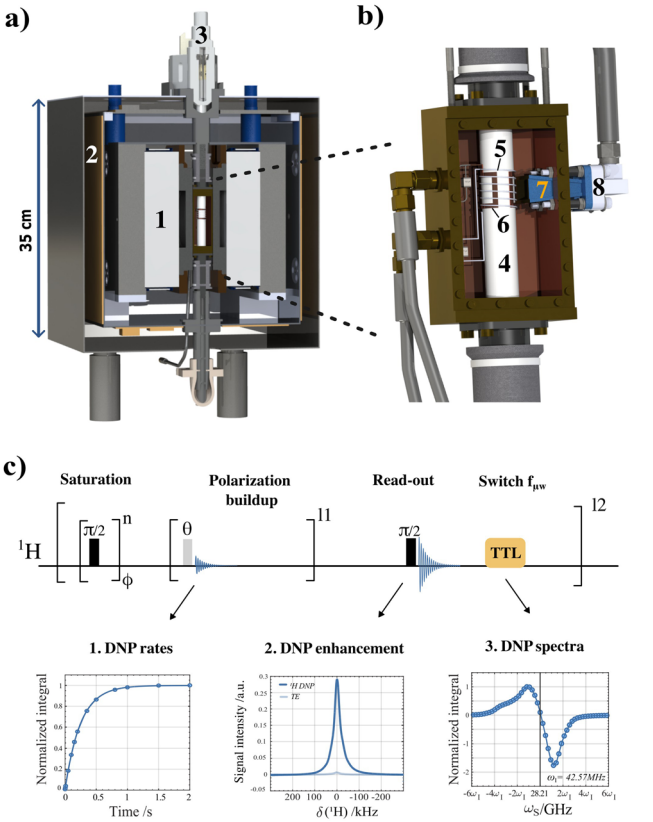

Fig. 2 Overview of the hardware and experimental design of the benchtop DNP polarizer. (a) Frontal cut of the prototype benchtop 1 T DNP polarizer co-developed by Bruker Biospin that was used for all of the DNP experiments. The polarizer is equipped with a 1 T permanent magnet (1) that is temperature stabilized at 301 K by 6 PID controlled heating mats (2) and a liquid nitrogen cryostat insert (3) that operates at 77 K. The cryostat itself is suited to fit a 4 mm EPR tube. (b) Transverse cut of the DNP NMR probe. A quartz tube (4) is used to hold the ^{13}C solenoid radiofrequency (rf) coil (5) and the ^{1}H saddle rf coil (6) which can be tuned externally to 10.7 MHz and 42.57 MHz respectively. A Kα-band microwave source is used to amplify microwave frequencies from 26.6 to 28.8 GHz up to 5 watts. A rectangular antenna horn (7) is placed as close as possible to the NMR coils and directs the microwaves onto the sample location after the coaxial to waveguide transition (8). (c) The pseudo-3d pulse sequence is shown that enabled us to extract the hyperpolarization build-up rates using small angle rf pulses (1), the DNP enhancement factors (2) together with the DNP spectra (3). More information is provided in the materials and methods section.

polarizer (Fig. 2a and b). Our goal is to optimize the nitroxide radical concentration immobilized in hyperpolarizing solids with the objective of generating as much polarization as possible in a timeframe (<1 s) compatible with future recyclable DNP applications. Moreover, we want to probe the underlying DNP mechanism at play when working at these optimal radical concentrations in HypFlow DNP conditions. This way, future design of the hyperpolarizing solids might be distinctively optimized to allow for larger enhancement factors, suitable polarization build-up rates, and finally longer relaxation times for more efficient dilution-free melting to be performed.

More specifically, signal enhancements and corresponding build-up rates together with their characteristic relaxation

times were measured for silica-immobilized nitroxide radical concentrations ranging from 20–74 μmol cm^{-3} and compared to solvated TEMPOL from 10–100 mM in a glassy state. At each set of radical concentrations, DNP spectra were also obtained by stepping the microwave frequency ($f_{\mu w}$) between 27.7 and 28.3 GHz and plotting it against the proton enhancement factor. A fully automated experimental and processing approach was used on the benchtop DNP polarizer (Fig. 2a and b) to reach this goal. In Fig. 2c, the methodology to do so is summarized and is based on a single pseudo-3d pulse sequence that was able to extract (i) the DNP build-up rates, (ii) the thermal and DNP hyperpolarized NMR spectra and (iii) the DNP spectra *via* MATLAB (MathWorks, Massachusetts, USA) using a processing pipeline that is available *via* the Zenodo repository.†

Finally, initial investigation into the main hyperpolarization transfer mechanisms responsible for DNP at 1 T and 77 K using nitroxide radicals was assisted by performing Q-band (1.2 T) continuous-wave (CW) EPR experiments. The EPR lineshape of 50 mM TEMPOL radical in frozen solution at 1.2 T was used to rationalize the shape of the DNP spectra. From this, conclusive remarks on the optimization and rationalization of performing DNP at 1 T and 77 K using nitroxide radicals in amorphous frozen solutions and immobilized states are contextualized with the prospect of advancing DNP into a recyclable hyperpolarization technique.

2. Results and discussion

To compare the DNP performances of nitroxide radicals at 1 T and under cryogenic measurement conditions of 77 K in amorphous and immobilized conditions, a series of TEMPOL concentrations ranging from 10–100 mM were dissolved using a partially protonated 2 : 2 : 6 H_2O : D_2O : DMSO-d_6 (v : v : v) solution (**1**) to allow for good glassing capabilities when flash-frozen. TEMPOL was chosen as the reference DNP radical due to its chemical stability, proven DNP performance, and high compatibility towards immobilization onto porous materials as immobilization is essential for the envisioned recyclable DNP application.[22,24,27]

For immobilizing the nitroxide radicals, commercially available silica beads with an average pore diameter of 5 nm (Fig. S1, ESI‡) were used to generate a set of silica-based hyperpolarizing solids with varying nitroxide radical concentrations ranging from 20–74 μmol cm^{-3} referred to as HYPSO-5. The material properties of the used hyperpolarizing solids are summarized in Table 1.[21] The exact pore volume of the HYPSO-5 samples was finally impregnated with a partially protonated 2 : 8 H_2O : D_2O (v : v) solution (**2**).

The main output of the systematic hyperpolarization study using the pseudo-3d pulse sequence shown in Fig. 2c is reported in Fig. 3a for the different nitroxide radical concentrations under amorphous frozen conditions and in Fig. 3b for the different immobilized nitroxide radicals concentrations. Based on the pulse sequence highlighted in Fig. 2c, DNP build-up rates (τ_{dnp}^{-1}) were measured at each $f_{\mu w}$ which was then stepped automatically to obtain the overall DNP spectra. Afterwards, the MATLAB-based processing pipeline provided the enhancement factors (Fig. 3-I and II) together with the corresponding build-up rates at both the positive and negative extrema (Fig. 3-III and IV) of the DNP spectra (Fig. 3-V). The automated and systematic approach minimized any external factors that potentially could hinder comparison of the DNP performances between radical concentrations. More detailed information on the sample preparation, NMR acquisition, DNP enhancement factor calculation, DNP build-up rate extraction and processing workflow can be found in the Materials and methods section and in the ESI.‡

Table 1 HYPSO-5 material properties including the porous volume (cm^3 g^{-1}) and measured pore diameter (nm) are reported. Their DNP performances are summarized based on the polarization enhancement factor and build-up rate (s^{-1}) as a function of immobilized TEMPO loading expressed in μmol cm^{-3}

[Nitroxide] (μmol cm^{-3})	Porous volume (cm^3 g^{-1})	Pore diameter (nm)	Enhancement	Build-up rate (s^{-1})
20	0.65	4	8	—
25	0.69	5	28	1.14 ± 0.19
43	0.63	4	42	0.94 ± 0.03
58	0.57	5	24	2.08 ± 0.18
74	0.55	4	19	2.08 ± 0.37

2.1. DNP enhancement factors

As shown in Fig. 3a-I and II, a maximal proton enhancement factor of 102 was obtained with solvated TEMPOL at a concentration of 50 mM using solution (**1**) after $f_{\mu w}$ optimization of 28.2 GHz and correction for the probe background (Fig. S2, ESI‡). With respect to the radical concentration, the enhancement shows a steep increase in amplitude from 10 mM up until 30 mM followed by a plateau until 50 mM with a fall-off in efficiency from 60 mM TEMPOL onward (the calculated enhancement at 70 mM is recognized as an outlier). For each concentration of TEMPOL, the maximal enhancement occurred systematically at the negative lobe of the DNP spectra (circles, red) and shows 25% higher polarization compared to optimal $f_{\mu w}$ inducing positive hyperpolarization (squares, blue). Overall, the dependency on concentration is analogues to what is observed under traditional dDNP conditions at 6.7 T and 1–4 K, yet in our case already at lower radical concentrations (>20 mM) enhancement starts reaching optimal values. The optimal DNP enhancement when using HYPSO-5 powders reaches a factor of 42 at a concentration of 43 μmol cm^{-3} using solution (2) as shown in Fig. 3b-I and II and reported in Table 1. The hyperpolarization dependency on the radical loading shows a narrower window of optimal concentrations when the nitroxide radicals are immobilized onto the silica matrix than when dissolved in solution before freezing. At a higher nitroxide concentration of 74 μmol cm^{-3}, the enhancement factor therefore drops below 20.

2.2. DNP build-up rates

The overall DNP build-up rates (τ_{dnp}^{-1}) in the benchtop DNP polarizer for different solvated and immobilized nitroxide

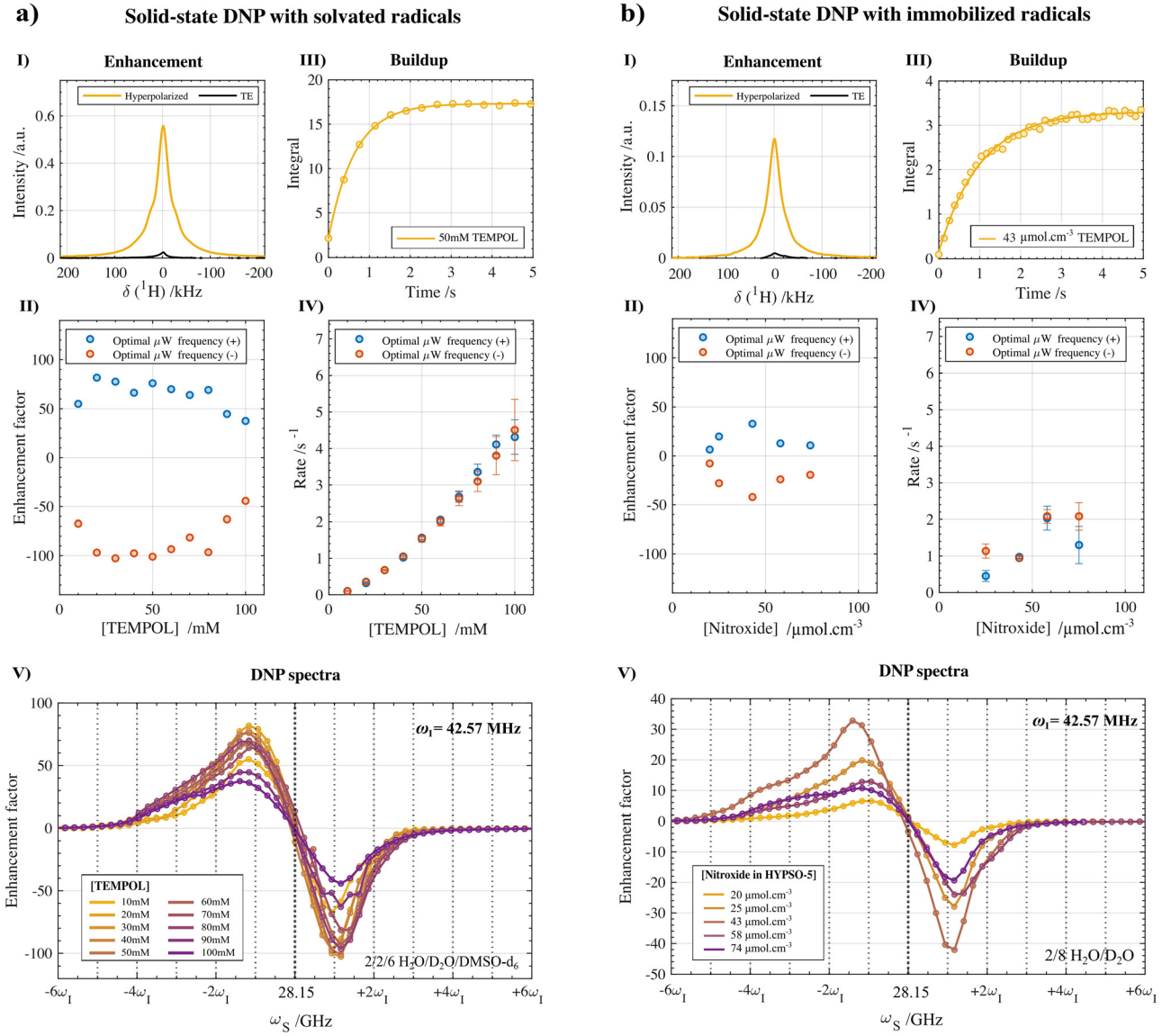

Fig. 3 Solid-state ^{1}H-DNP performances at 1 T and 77 K with varying concentrations of TEMPOL radicals (a) randomly distributed in an amorphous frozen solution (10–100 mM in a 2 : 2 : 6 H_2O : D_2O : DMSO-d_6 (v : v : v) solution) and (b) under chemically immobilized conditions in the HYPSO-5 silica mesoporous matrix (20–74 μmol cm^{-3} impregnated with a partially protonated 2 : 8 H_2O : D_2O (v : v) solution). A single pulse sequence (Fig. 2c) with the corresponding MATLAB processing pipeline (available in Zenodo†) enabled us to capture the thermal and DNP hyperpolarized NMR spectra (at the optimal $f_{\mu w}$) (I), the enhancement factors (II), the hyperpolarization build-up profiles (III), the corresponding rates τ_{dnp}^{-1} (IV) and the DNP spectra (V) in a single NMR experiment. The enhancement factors were calculated according to eqn (2) in the experimental section, while τ_{dnp}^{-1} were fitted using the monoexponential function shown in eqn (3) with typically 15 build-up points. The error boundaries correspond to a 95% confidence interval. More information about the processing and experimental parameters can be found in the Materials and methods section.

radical concentrations are plotted against each other in Fig. 3-IV. Specifically, the DNP rates that were measured at the optimal $f_{\mu w}$ for obtaining positive (circles, blue) and negative (circles, red) DNP optima are shown. The individual build-up curve of the optimal radical concentrations and microwave conditions are represented in Fig. 3-III. In general, the position of the $f_{\mu w}$ for optimal (−) DNP and (+) DNP did not seem to impact the bulk polarization transfer rate much. Both for the positive and negative maxima of the DNP spectra show in Fig. 3-IV, τ_{dnp}^{-1} was found to be equal within the error boundaries of the exponential fit for most radical concentrations (besides 25 μmol cm^{-3}). This statement can be generalized to any microwave frequency and to any nitroxide concentration either in a frozen solution or in HYPSO-5. In Fig. 4a this is illustrated by plotting τ_{dnp}^{-1} at each corresponding $f_{\mu w}$ for the 50 mM TEMPOL. Note that outside the $f_{\mu w}$ range where DNP is inefficient, τ_{dnp}^{-1} could not be fitted properly anymore as observed in Fig. 4b. The remaining concentrations for the solvated and immobilized nitroxide radicals are provided in Fig. S6 and S7 that are found in the ESI.‡

For solvated TEMPOL, a non-linear correlation of τ_{dnp}^{-1} with an increasing nitroxide concentration is also noticeable

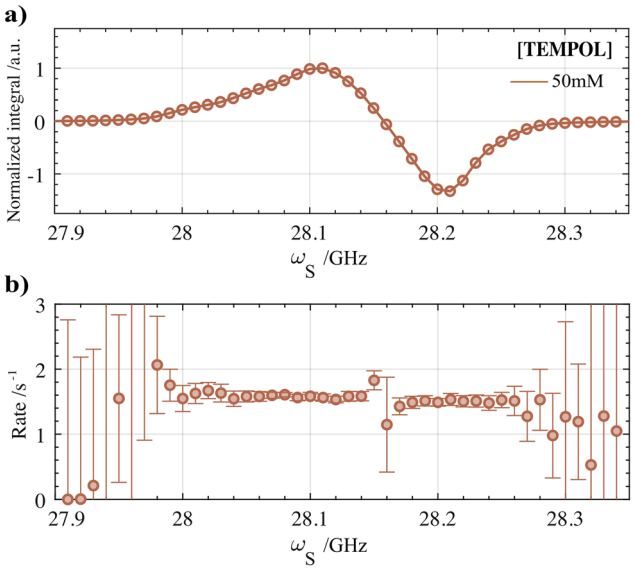

Fig. 4 (a) ^{1}H-DNP spectrum measured for the optimal TEMPOL concentration of 50 mM at 1 T and 77 K. (b) ^{1}H-DNP build-up rates (τ_{dnp}^{-1}) at each corresponding $f_{\mu w}$ of the DNP spectrum. τ_{dnp}^{-1} values were extracted using the MATLAB processing pipeline after correction for the background build-up (see Fig. S4 and S5 (ESI‡)). The same methodology was used for each nitroxide concentration in frozen solution or in the hyperpolarizing solids. The results are presented in Fig. S6 and S7 of the ESI.‡

in Fig. 3a-IV. In the benchtop DNP polarizer, τ_{dnp}^{-1} ranges from 0.2 s^{-1} for 10 mM TEMPOL towards 4.5 s^{-1} for 100 mM TEMPOL. By increasing the number of electrons (e) in the amorphous frozen solution, the dipolar interaction strength between electrons is influenced in particular. Assuming a random statistical distribution of electrons, the e–e dipolar interaction will increase proportionally with concentration as well.[36,37] This gives us the ability to gain insight into the dependency of τ_{dnp}^{-1} on the e–e dipolar interaction strength. In Fig. S3 (ESI‡), the relationship between the build-up time and the radical concentration was fitted with a simple non-linear model according to:

$$\tau_{dnp}^{-1} = \alpha C_e^{\lambda} \quad \text{with} \quad D_{ee} \propto C_e \tag{1}$$

where C_e represents the concentration of the radical, D_{ee} is the e–e dipolar interaction strength, α is the proportionality constant and λ is the exponent that empirically describes the relationship between τ_{dnp}^{-1} and C_e. The fitted value for the λ exponent was found to be 1.58 ± 0.03 as detailed in Fig. S3 of the ESI.‡ This relationship therefore gives a first indication that electron–electron interactions cannot be overlooked when discussing the polarization transfer mechanism for broad line radicals under these conditions later on.[38]

In the pores of HYPSO-5, the impact of varying the immobilized nitroxide concentration on τ_{dnp}^{-1} of the impregnated partially protonated solution (**2**) is less predictable than in the case of nitroxides in a glassy state. This can be noticed when comparing Fig. 3a-IV with Fig. 3b-IV. Instead of the monotonically increasing τ_{dnp}^{-1} for solvated nitroxides, the build-up rates for immobilized nitroxides feature a plateau when reaching higher concentrations. This is not entirely unexpected since during immobilization of the nitroxide precursor in the pores of HYPSO-5, effects such as clustering of the radicals are thought to be significant especially at higher radical loading. The consequences that the clustering has on DNP in hyperpolarizing solids are however not yet fully understood.[39]

At the optimal concentration of 43 μmol cm^{-3}, the polarization rate during $f_{\mu w}$ equals 0.94 ± 0.03 s^{-1}. When comparing this with typical ^{1}H build-up rates for HYPSO-5 under dissolution DNP conditions,[21] the gain in speed approximates two orders of magnitude, which is beneficial for limiting the total recycle time and therefore using it in the context of the future HypFlow DNP approach.

2.3. DNP spectra

The DNP spectra plotted for each of the nitroxide concentrations are overlayed in Fig. 3a-V. For the lowest concentration of 10 mM, a quasi-symmetrical positive and negative lobe of the DNP spectra is apparent separated by slightly more than 2 times the Larmor frequency (ω_I of 42.57 MHz) of the hyperpolarized proton nuclei under observation. A separate representation of the DNP spectra for each concentration is provided in Fig. S8 (ESI‡). Increasing to higher nitroxide concentrations gradually results in more asymmetry. In particular, for the positive lobe, a broader polarization enhancement profile becomes apparent at high nitroxide concentrations. One of the possible explanations could be that the high concentration of electrons is affecting the overall line shape of the EPR profile. This will in principle also be reflected in the DNP spectra. A general methodology for rationalizing the shape of the DNP spectra in these low-field conditions is given later (Fig. 6 and 7). However, deeper investigation to explain the change in ^{1}H-DNP spectra with radical concentration is planned for the future. This could include radical clustering effects or the influence of the increased e–e dipolar interactions at higher radical concentrations.

For HYPSO-5, an overlay of the measured DNP spectra after immobilizing different amounts of nitroxide radical on the mesoporous silica is shown in Fig. 3b-V and Fig. S9 (ESI‡) for a separate representation. The DNP spectra have a similar appearance as observed for solvated TEMPOL in frozen solution, again showing maximal and minimal hyperpolarization at respectively around $+\omega_I$ and $-\omega_I$. However, an overall lower proton enhancement factor is observed when comparing it with Fig. 3a-V where the performance of TEMPOL in an amorphous glassy state is shown. A completely random distribution of radicals which is believed to benefit DNP efficiency, cannot be guaranteed when immobilizing the TEMPOL derivative in the pores of HYPSO-5. However, as previously reported,[21] the pore geometry of HYPSO-5 has been tailored to imitate the random distribution of radicals compared to previous generations of structured silica-based hyperpolarizing solids with highly ordered porosity.[24,27]

Finally, the influence of $f_{\mu w}$ modulation on the DNP performance in the HYPSO-5 powders was also investigated. The beneficial effect of using $f_{\mu w}$ modulation was much more

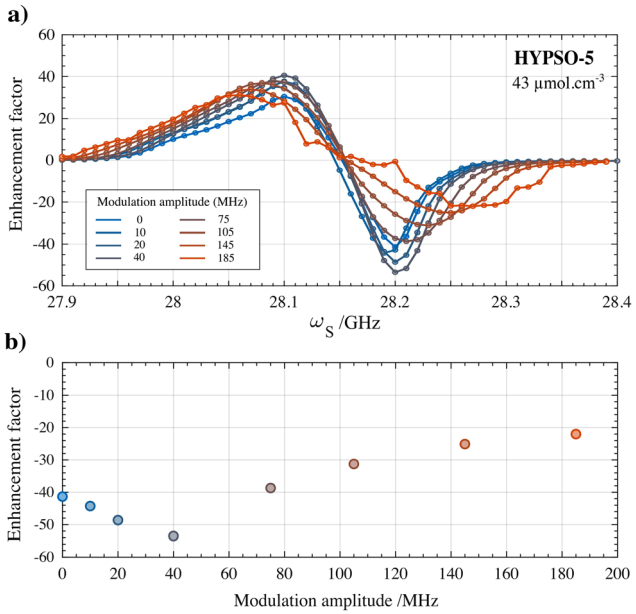

Fig. 5 (a) The influence of varying the microwave frequency modulation bandwidth $\Delta f_{\mu w}$ (0–185 MHz) on the ^{1}H-DNP spectrum (from 27.9 GHz to 28.4 GHz) measured on the best performing HYPSO-5 powder with a nitroxide concentration of 43 µmol cm^{-3}. In each experiment a microwave modulation frequency (f_{mod}) of 60 kHz with a triangle shape was used at the maximum output power of 5 watts. (b) A plot of the maximum negative enhancement factor deduced from the ^{1}H-DNP spectrum plotted against different $\Delta f_{\mu w}$. An optimum enhancement of 56 is reached at $\Delta f_{\mu w}$ of 40 MHz.

pronounced in HYPSO-5 powders (>25% increase) than for the glassy solution where it did not improve DNP substantially. Inhomogeneities in radical distribution in HYPSO-5 can lead to inefficient spectral diffusion compared to radicals in a glassy frozen solution. Frequency modulation thus could potentially compensate for a lack of spectral diffusion in some regions of the HYPSO-5 powder. Fig. 5a shows the effect of varying the frequency modulation bandwidth $\Delta f_{\mu w}$ on the DNP spectrum of the best performing HYPSO-5 powder with 43 µmol cm^{-3} of nitroxide radical loading. In Fig. 5b, the polarization enhancement at optimal DNP is plotted. A maximum enhancement of 56 is reached at $\Delta f_{\mu w}$ of 40 MHz using a modulation frequency (f_{mod}) of 60 kHz with a triangular shape. With further increasing $\Delta f_{\mu w}$, the enhancement factor drops. The DNP spectra become broader and less resolved as seen in Fig. 5a. The reason is the simultaneous generation of both positive and negative nuclear spin hyperpolarization due to the large $f_{\mu w}$ irradiation bandwidth. Note that the overall comparison made in Fig. 3a-V was done without the use of any $f_{\mu w}$ modulation to ensure reliable comparison of the DNP characteristics of nitroxide radicals under solvated and immobilized conditions.

2.4. DNP mechanism for polarization transfer

Insights into the polarization transfer mechanism which is dominant when performing DNP can be crucial for tailoring the radicals used for hyperpolarization. In high-field MAS-DNP, large research efforts have been made in this regard where the cross effect mechanism has been determined to be the dominant DNP mechanism for broad nitroxide-based radicals at optimal concentrations.[40–42] We found a first set of indications that when performing static solid-state DNP using optimized TEMPOL concentrations at 1 T and 77 K, the cross effect polarization transfer mechanism should also be taken into account.

The indications are based on rationalizing the shape of the ^{1}H DNP spectra in Fig. 3(V) for either solid effect or cross effect. The line shape is based on the expected EPR profile of 50 mM solvated TEMPOL in frozen solution at 1 T and 77 K. For this, first a continuous-wave (CW) EPR measurement shown in Fig. 6a was performed on an identical 50 mM TEMPOL frozen solution under similar conditions of 1.2 T (Q-band, 34 GHz) and 77 K. The resulting EPR spectrum is shown in Fig. 6b. After fitting the CW-EPR spectrum using the Easyspin MATLAB package,[43] the anisotropic *g*-tensor and hyperfine *A*-tensor values were extracted together with the homogeneous broadening parameters for 50 mM TEMPOL (Table 2).

Afterwards, the extracted parameters were used to predict the $f_{\mu w}$-swept EPR profile for 50 mM TEMPOL under HypFlow DNP conditions shown in Fig. 6c. The exact conditions in which the benchtop DNP polarizer was operating were derived from the chemical shift of the solid-state proton peak (ω_I = 42.669 MHz which corresponds to a field of 1.0022 T). A detailed description on the EPR experiment and fitting procedure can be found in the Materials and methods section. The large anisotropy of the *g*-tensor and hyperfine tensor due to the spin-1 ^{14}N nucleus results in the large inhomogeneous broadening spanning over 350 MHz as can be seen in Fig. 6c. Especially at low temperatures (1–4 K) and moderate magnetic fields (up to 7 T) these EPR properties have been recognized to enable effective hyperpolarization of high-gamma nuclei such as protons by means of thermal mixing induced polarization transfer.[44–47] However, in a magnetic field of 1 T and at an operating temperature of 77 K, field- and temperature-dependent electronic and nuclear interactions including their relaxation rates change, reducing the thermal mixing efficiency, making room for the solid effect or cross effect polarization transfer to become dominant.[48–50]

While for narrow line radicals the resulting DNP spectra and optimal $f_{\mu w}$ positions can be discriminated for either the solid effect or cross effect case, for broad line radicals this becomes less straightforward.[51] We therefore attempted to rationalize the corresponding DNP spectra inspired by the electron bin model in the case of TEMPOL described in Kundu *et al.*[52] For now, we chose to disregard any effect of hole burning or spectral diffusion to remain in scope of the paper.[38,52] By discretizing the EPR profile in 1024 points, an estimation of the shape of the DNP spectrum assuming the solid effect and cross effect could be calculated using respectively eqn (4) and (5) available in the Materials and methods section. After implementing the correct matching condition, the experimental DNP spectrum acquired for 50 mM TEMPOL in a glassy frozen solution was compared to the resulting DNP spectra simulations. The results of this analysis are shown in Fig. 7.

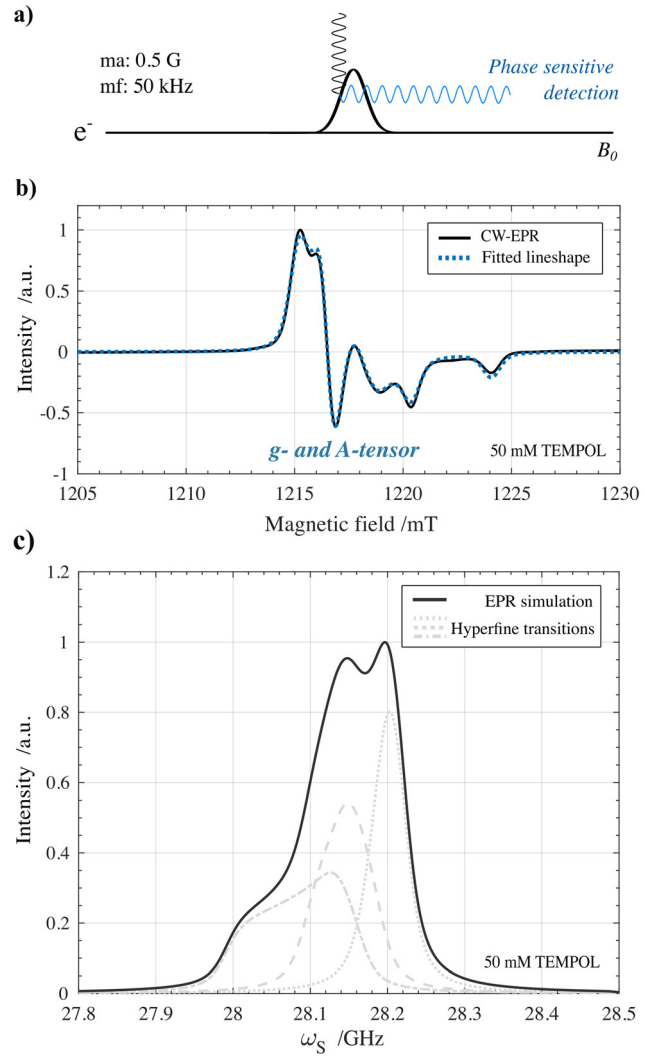

Fig. 6 (a) Phase-sensitive continuous wave (CW)-EPR experiment measured *via* sweeping the magnetic field with a field modulation amplitude (ma) of 0.5 G and a modulation frequency (mf) of 50 kHz. (b) Q-band CW-EPR spectrum of the optimal 50 mM TEMPOL radical DNP solution (**1**) measured at 1.2 T and 77 K. The Easyspin MATLAB package was used to extract the anisotropic *g*-tensor and hyperfine *A*-tensor values at 1.2 T. (c) A simulated frequency-swept EPR spectrum of 50 mM TEMPOL to rationalize the EPR profile used for performing DNP at a benchtop polarizer with a specific field of 1.0022 T (ω_I = 42.669 MHz). The contribution of the ^{14}N hyperfine transitions to the overall simulated EPR spectrum is also visualized in dotted, striped, and dotted-striped lines. See the Materials and methods section for more detailed information on the EPR measurements.

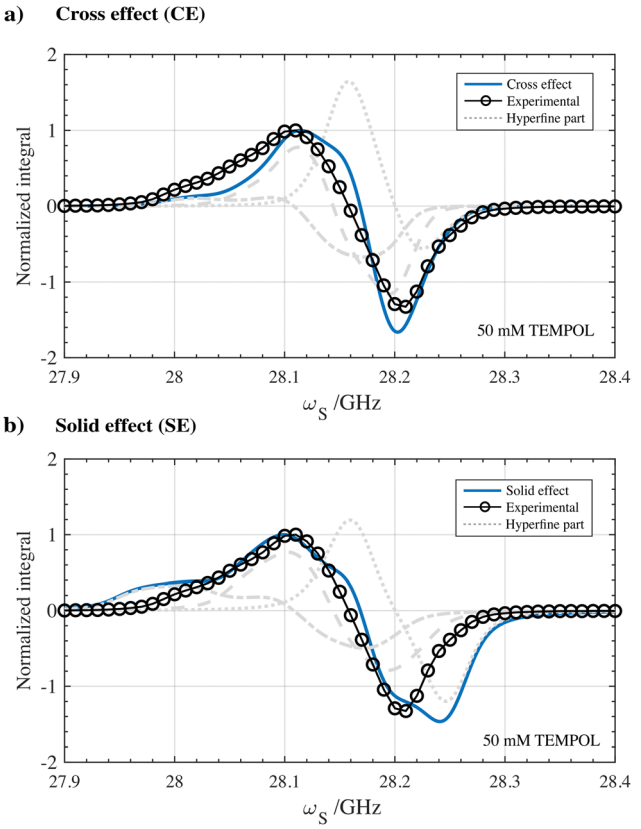

Fig. 7 Simulated ^{1}H DNP spectra assuming (a) cross effect and (b) solid effect type of polarization transfer using 50 mM TEMPOL in a partially protonated frozen glassy solution at 77 K and 1 T. The calculated line shapes assuming the cross effect and solid effect are overlayed with the experimental ^{1}H DNP spectrum as a comparison. Solid-state EPR simulations of TEMPOL at 1.0022 T were performed using the Easyspin MATLAB package and based on experimental CW-EPR measured at 1.2 T as can be seen in Fig. 6. The ^{1}H-DNP spectrum simulations are based on a straightforward analytical electron bin model assuming monochromatic microwave hole burning without spectral diffusion. Detailed information on the acquisition and simulation of the DNP spectra can be found in the Materials and methods section.

Table 2 Fitted *g*-tensor and hyperfine *A*-tensor values for 50 mM TEMPOL extracted from the experimental CW-EPR spectrum shown in Fig. 6b

Inhomogeneous broadening (Δ)				Homogeneous broadening (δ)	
g-tensor (unitless)		*A*-tensor (MHz)		Lorentzian (MHz)	Gaussian (MHz)
g_{xx}	2.008	A_{xx}	24.23	17.65	15.63
g_{yy}	2.005	A_{yy}	16.96		
g_{zz}	2.001	A_{zz}	103.33		

Despite the simplicity of the model, the calculated DNP spectrum assuming the cross effect shown in Fig. 7a seems to reflect the characteristics of the experimental ^{1}H DNP spectrum. In particular, the position and shape of the negative lobe of the calculated DNP spectrum are in better agreement. In contrast, assuming the solid effect, the calculated DNP spectrum illustrated in Fig. 7b shows a broader DNP profile with polarization being generated up to 28.25 GHz. The DNP simulations presented in Fig. 7 together with the non-linear dependency of the DNP build-up rate on the radical concentration shown in Fig. 3a-IV are therefore a first set of indications that the cross effect seems an important contributor to enhancing nuclear spins at 1 T and 77 K using solvated nitroxide radicals. Surprisingly, the cross effect seems dominant over the entire range of nitroxide concentration from 10–100 mM, while one would expect solid effect contributions to become more significant at lower concentrations.[48] However, in Fig. 2a-V, the position of the DNP optima and the overall shape of the DNP

profiles are only slightly influenced by the radical concentration. Which minimum nitroxide concentration is required for the cross effect to be dominant over the solid effect could therefore be an interesting question to solve in the future. Finally, the experimental solid-state DNP spectra measured for solvated 50 mM TEMPOL and for 43 μmol cm^{-3} HYPSO-5 are overlayed and showcased in Fig. S10 (ESI‡). The overlapping line shape could be an indication that, also when using hyperpolarizing solids at benchtop conditions, cross effect polarization transfer from the dipolar coupled electrons on the surface of the pores needs to be considered. Yet, more definite insights can only be realized when considering all other processes impacting DNP such as spectral diffusion, spin diffusion and paramagnetic induced relaxation. This is aimed for future investigation.

3. Conclusions

Optimization of the radical concentration used in a benchtop DNP polarizer operating at 1 T and 77 K has indicated that for HYPSO-5 an optimal loading of 43 μmol cm^{-3} nitroxide radical gives proton polarization enhancement inside the pores up to 56 in under a second. Solvated nitroxide radicals in the form of TEMPOL embedded in frozen solution, even allows for proton enhancement factors up to 100 for the optimal concentration of 50 mM. This is particularly promising in view of future HypFlow DNP applications. Two-dimensional experiments can benefit from a fast recycle time giving an approximate acquisition time of 10 minutes for 2D liquid-state hyperpolarized experiments with 512 transients. Moreover, we found the first indications that DNP using broad line nitroxide radicals at a low-magnetic field and high temperatures is dominated by cross effect polarization transfer. This indication includes analytical cross effect DNP spectrum simulations derived from the Q-band EPR profile of TEMPOL that agree well with the experimentally obtained ^{1}H DNP spectrum. Future optimization of hyperpolarizing solids towards cross effect DNP will therefore benefit our goal to achieve recyclable hyperpolarization that is produced under accessible conditions.

4. Materials and methods

4.1. ^{1}H-DNP experiments at 1 T and 77 K

4.1.1. Sample formulation for solvated radicals. A glass-forming solution with the following volumetric ratio 2 : 2 : 6 H_2O : D_2O : DMSO-d_6 (v : v : v) (**1**) was doped with varying quantities of a stock polarizing agent solution containing TEMPOL radicals to finally generate 10 samples with a varying nitroxide concentration of 10 mM to 100 mM in steps of 10 mM. All chemicals were purchased from Sigma-Aldrich and the deuteration purity for D_2O and DMSO-d_6 were respectively 99.5% and 99.96%. This sample formulation with the corresponding preparation procedure ensured good amorphous glass-forming capabilities to end up with a random distribution of radicals. The final amount of proton spins eligible for DNP hyperpolarization amounts to a concentration of 22 M. Finally, by filling a 4 mm (o.d.) Wilmad quartz EPR sample holder with 200 μL of the ^{1}H DNP test solution, the solid-state DNP performances at 1 T and 77 K could be benchmarked according to the experimental design described later.

4.1.2. Sample formulation for hyperpolarizing solids. In hyperpolarizing solids (HYPSOs), the radical polarizing agents are immobilized on the surface of a mesoporous material instead of being randomly distributed in an amorphous frozen solution. A selection of HYPSO-5 silica-based matrices derived from commercially available mesoporous silica beads (Silia*Sphere*™) with a varying concentration of immobilized nitroxide radicals from 20–74 μmol cm^{-3}, all with an average pore diameter of around 5 nm, was chosen to benchmark the DNP performance at 1 T and 77 K. The reason for this choice of particular family of hyperpolarization solids is their excellent DNP performance at 6.7 T and 1–4 K. A summary of the HYPSO-5 material properties including porous volume and the final concentration of immobilized nitroxide radicals can be found in Table 1. For a full and detailed description of the preparation procedure of the HYPSO-5 materials, the reader is referred to Cavaillès *et al.*[21] and the ESI.‡ Finally, a partially protonated 2 : 8 H_2O : D_2O (v : v) solution (**2**) amounting to the total pore volume (determined *via* N_2 physisorption) of each of the HYPSO-5 samples (Table 1) was impregnated in approximately 40 mg of the corresponding powder using an incipient wetness impregnation technique with continuous stirring, until the sample appeared dry again. No DMSO-d_6 was required since the amorphous distribution of radicals which is beneficial for DNP is already achieved by immobilization *via* silica coating. The 2 : 8 ratio between H_2O and D_2O gave rise to 0.88 mmol of proton spins available for DNP hyperpolarization under immobilized conditions of radicals.

4.1.3. Benchtop DNP polarizer. The DNP measurements shown in Fig. 3 were performed using a prototype solid-state DNP polarizer co-developed with Bruker as shown in Fig. 2 and 8. The DNP polarizer is equipped with (i) a temperature-controlled permanent 1 T magnet, (ii) a liquid nitrogen cryostat insert operating at 77 K, (iii) a home-build ^{1}H/^{13}C NMR probe composed of a saddle and solenoid coil with orthogonal B_1 field resonating at the frequencies of 42.57 MHz and 10.7 MHz respectively, and (iv) a solid-state Kα-band microwave synthesizer that amplifies microwave frequencies from 26.6 to 28.8 GHz up to 5 watts. Frequency modulation with a maximal bandwidth amplitude ($\Delta f_{\mu w}$) and frequency (f_{mod}) of 200 MHz and 100 kHz respectively could be modified manually. A triangular shape modulation was used in case frequency modulation was activated during DNP. More information on the design and specifications of the setup can be found in Bocquelet *et al.*[30]

4.1.4. Experimental design. One of the main objectives of this work was benchmarking the DNP performances of varying concentrations of TEMPOL radicals at 1 T and 77 K either under amorphous conditions in a frozen glassy state or under chemically immobilized conditions in a silica mesoporous matrix. Therefore, a single DNP benchmarking pulse sequence visualized in Fig. 2c of the manuscript was constructed to

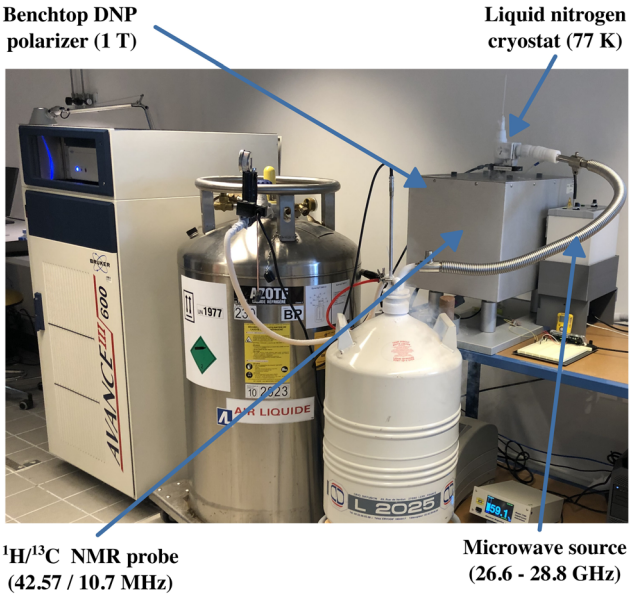

Fig. 8 A visual representation of the entire benchtop DNP polarizer setup. The location of the main hardware components (the magnet, the cryostat, the microwave source, the DNP-NMR probe) are highlighted using arrows.

capture the (i) thermal and DNP hyperpolarized NMR spectra, (ii) the hyperpolarization build-up profiles and (iii) the DNP spectra in a single NMR experiment for each of the radical concentrations used.

Specifically, the benchmarking protocol started with a saturation block using hard $\pi/2$ rf-pulses with alternating phases that are separated by a short delay and repeated 50 times. After destroying the residual magnetization on the proton rf-channel, the hyperpolarization build-up was monitored *via* a small $\pi/36$ flip angle rf-pulse that allowed us to trace the ^{1}H-NMR signal. A total of 15 small angle rf-pulses were typically used to monitor the build-up with a delay that was depending on the DNP rate. Note that during the entire duration of the pulse sequence the microwave was switched on at maximum power (5 W) since no TTL gating was available. After the build-up sequences, a hard $\pi/2$ rf-pulse was used to maximize the detected hyperpolarized signal for finally constructing the DNP spectra and calculating the enhancement factor (*vide infra*). Finally, a TTL pulse generated by the NMR console positioned after the final acquisition was read by an Arduino board to trigger the microwave source to change frequency by 10 MHz during a given delay of 5 s, after which the pulse sequence reinitialized its saturation and detection cycle. The $f_{\mu w}$ was swept from 27.8 to 28.44 GHz and generated 65 separate DNP build-ups (15 FID's) and a single ^{1}H-NMR spectrum (1 FID) in series, thus resulting in 1040 transients in the pseudo F1 dimension. Since the DNP build-up rates are considerably fast at optimal nitroxide concentrations (around 2 s^{-1} for 50 mM), the total acquisition time for fully benchmarking the DNP samples was on average 12 minutes. For the lower radical concentration samples, the total acquisition time was prolonged up to 72 minutes.

A MATLAB-based processing pipeline, available in the ESI,‡ automatically rearranged the F1 dimension into the small and large flip-angle 1D NMR spectra which after integration generates the DNP build-up plots and the DNP spectra shown in Fig. 3. The signal enhancement factors were calculated according to the following formula:

$$\varepsilon_{\mathrm{DNP}} = \frac{I^{\mathrm{dnp}} - I^{\mathrm{thermal}}}{I^{\mathrm{thermal}} - I^{\mathrm{background}}}, \quad (2)$$

where I^{dnp} is the integration value of the hyperpolarized signal and I^{thermal} is the first integral of the DNP spectrum equal to the thermal equilibrium solid-state signal due to the off-resonant microwave irradiation. Due to considerable probe background in the ^{1}H-channel for the thermal signal, a correction was required considering the background contribution. In Fig. S2 of the ESI,‡ an overlay of the probe background with the total NMR signal in both the solvated and immobilized nitroxide radical case is given. The percentages of the background varied from 50% to 60% percent of the thermal equilibrium signal.

Next, the extraction of the build-up rates was performed by fitting the integrated small flip-angle signals (I_t^{dnp}) according to the exponential build-up:

$$I_t^{\mathrm{dnp}} = I_{\infty}^{\mathrm{dnp}}\left(1 - \exp\left(-\frac{t}{\tau_{\mathrm{dnp}}}\right)\right), \quad (3)$$

where τ_{dnp} is the characteristic DNP build-up time. The error margins in Fig. 3-IV correspond to a 95% certainty interval. To account for the background contribution obscuring the hyperpolarization build-ups, the first fit at off-resonant microwave frequency was subtracted from the other build-ups. Despite the background contribution, the final rates thus reflect the hyperpolarization build-up with the most precision as can be noticed in the ESI,‡ where the individual build-ups for each microwave frequency in the case of 50 mM TEMPOL are plotted without and with background subtraction respectively in Fig. S4 and S5 (ESI‡).

Finally, the DNP spectra were constructed based on the enhancement factor calculation of eqn (2). Additionally, to counteract a drift of the magnetic field due to potential temperature instabilities in the magnet, the microwave frequency values used for constructing the DNP spectra were corrected according to the Larmor frequency of the ^{1}H signal. Also, to make sure the absolute integration values (I^{dnp}) were consistent over the different concentrations, all processing was performed using 8k datapoints in the F2 dimension and the same exponential line broadening of 1 kHz. Since the MATLAB processing pipeline only imported frequency domain NMR data, the fast Fourier transform, and line broadening were performed using Topspin.

4.2. Q-band EPR experiments at 1.2 T and 77 K

4.2.1. Sample formulation and preparation. The CW EPR experiments were carried out with TEMPOL in frozen DNP solution, identical to the solution used in DNP benchmarking experiments capable of glass formation. TEMPOL (4-hydroxy-2,2,6,6-tetramethylpiperidin-1-oxyl), ≥97% total nitrogen (N)

basis, and DMSO-d_6 (hexadeuterodimethyl sulfoxide), 99% were purchased from Sigma-Aldrich, Merck KGaA, Darmstadt, Germany. A stock solution of 100 mM TEMPOL was first prepared by dissolving 3.516 mg of TEMPOL into 204.1 μL into the glass-forming solute with a volumetric ratio of 2 : 2 : 6 H_2O : D_2O : DMSO-d_6 (v : v : v). After dilution to the desired radical concentration (50 mM), 1 μL of the DNP solution was taken in a 1.6 mm (o.d.) quartz tube to perform the EPR experiments.

4.2.2. Instrumentation. EPR experiments were performed at 77 K and 34 GHz/1.2 T/51 MHz on a Bruker Elexsys E580 spectrometer with Q-band extension (SuperQ-FT-u bridge). The EN 5107D2 EPR/ENDOR probe with a dielectric resonator capable of performing both CW and pulse EPR experiments was used. The sample temperature was kept at 77 K using a CF 935 flow cryostat (Oxford Instruments) and liquid helium as a cryogen.

4.2.3. Experimental design

4.2.3.1. CW EPR. Field-swept CW EPR experiments were conducted with a field modulation amplitude of 0.5 G at a modulation frequency of 50 kHz for phase-sensitive detection of the reflected microwave signal. The microwave power was set to 60 μW (25 dB attenuation), and the microwave frequency was 34.1842 GHz.

4.3. DNP simulations

First, the anisotropic *g*- and *A*-tensor and homogeneous broadening parameters for the 50 mM TEMPOL sample were derived by fitting the experimental CW Q-band EPR measurement (1.2 T, 34 GHz) on an identical sample. Afterwards, an Easyspin[43] simulated frequency-swept EPR profile was simulated at the exact magnetic field of 1.0022 T (deduced from ω_I) in which the DNP spectrum was acquired. The resulting electron density profile was discretized into N = 1024 points, for which the following equations[52,53] were used to calculate the shape of the DNP spectrum assuming solid effect and cross effect respectively:

$$P_{I,j}^{SE}(\omega_s) = \left[h_{j+\Delta j}\frac{P_{S,j+\Delta j} - P_{S,j}}{1 - P_{S,j}P_{S,j+\Delta j}} - h_{j-\Delta j}\frac{P_{S,j-\Delta j} - P_{S,j}}{1 - P_{S,j}P_{S,j-\Delta j}}\right], \quad (4)$$

and

$$P_{I,j}^{CE}(\omega_s) = \left[h_j h_{j+\Delta j}\frac{P_{S,j+\Delta j} - P_{S,j}}{1 - P_{S,j}P_{S,j+\Delta j}} - h_j h_{j-\Delta j}\frac{P_{S,j-\Delta j} - P_{S,j}}{1 - P_{S,j}P_{S,j-\Delta j}}\right], \quad (5)$$

where $P_{I,j}$ is the relative average polarization of nuclear spins enhanced by the number of electrons h_j in point $N = j$ and $h_{j+\Delta j}$ in point $N = j + \Delta j$ derived from the normalized EPR spectrum at 1 T. Δj represents the shift in number of points that is required to match the frequency difference of the electron pair to the Larmor frequency ω_I of the nuclear spin under observation. $P_{S,j}$ is the polarization of electrons during microwave irradiation which is assumed to be equal to 0 at ω_s and equal to the thermal polarization at all other frequencies (monochromatic irradiation). The scripts for performing the simulations are available in the Zenodo repository.†

Author contributions

SJ conceived the project. EV and QS supervised the work performed. EV, CB, LB, and NR performed the experimental work. HNL synthesized the hyperpolarizing solids used in this work under the supervision of CT and LV. SVK, SAJ and GM provided the Q-band CW-EPR measurements on TEMPOL. JK, DB and RM provided the prototype benchtop DNP polarizer and further technological and scientific support. EV wrote the manuscript and all authors contributed to refining the manuscript.

Data availability

The main data reported in the manuscript consists of NMR and EPR data for which the raw data is available in the Zenodo repository: **https://zenodo.org/records/11120019**. The DOI is also included in the main manuscript. The data folder contains the raw NMR and EPR data used in the manuscript to benchmark the DNP performance of different hyperpolarizing solids containing various nitroxide radical loadings compared against the DNP performance of varying nitroxide concentrations (10–100 mM) solvated in a glassy frozen solution. The NMR data is formatted in a pseudo-3d data Bruker format. The EPR data is formated in a text file. The code folder contains the script to process the pseudo-3d data to extract the DNP parameters. The code folder also contains the script to estimate the lineshape of the DNP spectra in the solid effect and cross effect case using the EPR data as input.

Conflicts of interest

There are no conflicts to declare. The authors declare no competing financial interest. JK, DB and RM are employees of Bruker who co-developed the benchtop 1 T DNP prototype polarizer system.

Acknowledgements

We acknowledge Bruker Biospin for providing the prototype benchtop DNP polarizer. We additionally acknowledge C. Jose and C. Pages for use of the ISA Prototype Service, and S. Martinez of the UCBL mechanical workshop for machining parts of the experimental apparatus. This research was supported by ENS-Lyon, the French CNRS, Lyon 1 University, the Deutsche Forschungsgemeinschaft (Grant No: SFB 1527, Project No. 454252029), the European Research Council under the European Union's Horizon 2020 research and innovation program (ERC Grant Agreements No. 101044726/HypFlow) and the French National Research Agency (project 'HyMag' ANR-18-CE09-0013).

References

1 C. K. Larive, G. A. Barding and M. M. Dinges, *Anal. Chem.*, 2015, **87**, 133–146.

2 T. W.-M. Fan, *Prog. Nucl. Magn. Reson. Spectrosc.*, 1996, **28**, 161–219.
3 J. Marchand, E. Martineau, Y. Guitton, G. Dervilly-Pinel and P. Giraudeau, *Curr. Opin. Biotechnol.*, 2017, **43**, 49–55.
4 V. Ribay, C. Praud, M. P. M. Letertre, J.-N. Dumez and P. Giraudeau, *Curr. Opin. Chem. Biol.*, 2023, **74**, 102307.
5 J.-N. Dumez, J. Milani, B. Vuichoud, A. Bornet, J. Lalande-Martin, I. Tea, M. Yon, M. Maucourt, C. Deborde, A. Moing, L. Frydman, G. Bodenhausen, S. Jannin and P. Giraudeau, *Analyst*, 2015, **140**, 5860–5863.
6 L. Sellies, I. Reile, R. L. E. G. Aspers, M. C. Feiters, F. P. J. T. Rutjes and M. Tessari, *Chem. Commun.*, 2019, **55**, 7235–7238.
7 S. Jannin, J.-N. Dumez, P. Giraudeau and D. Kurzbach, *J. Magn. Reson.*, 2019, **305**, 41–50.
8 C. Hilty and S. Bowen, *Org. Biomol. Chem.*, 2010, **8**, 3361–3365.
9 B. Plainchont, P. Berruyer, J.-N. Dumez, S. Jannin and P. Giraudeau, *Anal. Chem.*, 2018, **90**, 3639–3650.
10 A. Abragam and M. Goldman, *Rep. Prog. Phys.*, 1978, **41**, 395–467.
11 G. R. Khutsishvili, *Phys.-Usp.*, 1966, **8**, 743.
12 J. H. Ardenkjær-Larsen, B. Fridlund, A. Gram, G. Hansson, L. Hansson, M. H. Lerche, R. Servin, M. Thaning and K. Golman, *Proc. Natl. Acad. Sci. U. S. A.*, 2003, **100**, 10158–10163.
13 K. Singh, C. Jacquemmoz, P. Giraudeau, L. Frydman and J.-N. Dumez, *Chem. Commun.*, 2021, **57**, 8035–8038.
14 J. Eills, D. Budker, S. Cavagnero, E. Y. Chekmenev, S. J. Elliott, S. Jannin, A. Lesage, J. Matysik, T. Meersmann, T. Prisner, J. A. Reimer, H. Yang and I. V. Koptyug, *Chem. Rev.*, 2023, **123**, 1417–1551.
15 W. E. Blumberg, *Phys. Rev.*, 1960, **119**, 79–84.
16 A. Abragam, V. Bouffard and Y. Roinel, *J. Magn. Reson.*, 1969, **1976**(22), 53–63.
17 I. J. Lowe and D. Tse, *Phys. Rev.*, 1968, **166**, 279–291.
18 C. D. Jeffries, *Proc. Phys. Soc.*, 1966, **88**, 257–258.
19 P. R. Vasos, A. Comment, R. Sarkar, P. Ahuja, S. Jannin, J.-P. Ansermet, J. A. Konter, P. Hautle, B. van den Brandt and G. Bodenhausen, *Proc. Natl. Acad. Sci. U. S. A.*, 2009, **106**, 18469–18473.
20 X. Ji, A. Bornet, B. Vuichoud, J. Milani, D. Gajan, A. J. Rossini, L. Emsley, G. Bodenhausen and S. Jannin, *Nat. Commun.*, 2017, **8**, 1–7.
21 M. Cavaillès, A. Bornet, X. Jaurand, B. Vuichoud, D. Baudouin, M. Baudin, L. Veyre, G. Bodenhausen, J.-N. Dumez, S. Jannin, C. Copéret and C. Thieuleux, *Angew. Chem., Int. Ed.*, 2018, **57**, 7453–7457.
22 D. Gajan, A. Bornet, B. Vuichoud, J. Milani, R. Melzi, H. A. van Kalkeren, L. Veyre, C. Thieuleux, M. P. Conley, W. R. Grüning, M. Schwarzwälder, A. Lesage, C. Copéret, G. Bodenhausen, L. Emsley and S. Jannin, *Proc. Natl. Acad. Sci. U. S. A.*, 2014, **111**, 14693–14697.
23 K. Nishimura, H. Kouno, Y. Kawashima, K. Orihashi, S. Fujiwara, K. Tateishi, T. Uesaka, N. Kimizuka and N. Yanai, *Chem. Commun.*, 2020, **56**, 7217–7232.
24 D. L. Silverio, H. A. van Kalkeren, T.-C. Ong, M. Baudin, M. Yulikov, L. Veyre, P. Berruyer, S. Chaudhari, D. Gajan, D. Baudouin, M. Cavaillès, B. Vuichoud, A. Bornet, G. Jeschke, G. Bodenhausen, A. Lesage, L. Emsley, S. Jannin, C. Thieuleux and C. Copéret, *Helv. Chim. Acta*, 2017, **100**, e1700101.
25 S. F. J. Cox, S. F. J. Read and W. T. Wenchebach, *J. Phys. C-Solid State Phys.*, 1977, **10**, 2917.
26 T. El Daraï, S. F. Cousin, Q. Stern, M. Ceillier, J. Kempf, D. Eshchenko, R. Melzi, M. Schnell, L. Gremillard, A. Bornet, J. Milani, B. Vuichoud, O. Cala, D. Montarnal and S. Jannin, *Nat. Commun.*, 2021, **12**, 1–9.
27 D. Baudouin, H. A. van Kalkeren, A. Bornet, B. Vuichoud, L. Veyre, M. Cavaillès, M. Schwarzwälder, W.-C. Liao, D. Gajan, G. Bodenhausen, L. Emsley, A. Lesage, S. Jannin, C. Copéret and C. Thieuleux, *Chem. Sci.*, 2016, **7**, 6846–6850.
28 T. Cheng, M. Mishkovsky, M. J. N. Junk, K. Münnemann and A. Comment, *Macromol. Rapid Commun.*, 2016, **37**, 1074–1078.
29 R. Kircher, H. Hasse and K. Münnemann, *Anal. Chem.*, 2021, **93**, 8897–8905.
30 C. Bocquelet, N. Rougier, H.-N. Le, L. Veyre, C. Thieuleux, R. Melzi, A. Purea, D. Banks, Q. Stern, E. Vaneeckhaute and S. Jannin, *ChemRxiv*, preprint, 2024, DOI: **10.26434/chemrxiv-2024-3nlndn**.
31 R. Kircher, S. Mross, H. Hasse and K. Münnemann, *Molecules*, 2022, **27**, 6402.
32 M. Sharma, G. Janssen, J. Leggett, A. P. M. Kentgens and P. J. M. van Bentum, *J. Magn. Reson.*, 2015, **258**, 40–48.
33 C.-G. Joo, K.-N. Hu, J. A. Bryant and R. G. Griffin, *J. Am. Chem. Soc.*, 2006, **128**, 9428–9432.
34 P. J. M. van Bentum, M. Sharma, S. G. J. van Meerten and A. P. M. Kentgens, *J. Magn. Reson.*, 2016, **263**, 126–135.
35 L. Frydman and D. Blazina, *Nat. Phys.*, 2007, **3**, 415–419.
36 N. Bloembergen, *Physica*, 1949, **15**, 386–426.
37 O. S. Leifson and C. D. Jeffries, *Phys. Rev.*, 1961, **122**, 1781–1795.
38 K. Kundu, A. Feintuch and S. Vega, *J. Phys. Chem. Lett.*, 2018, **9**, 1793–1802.
39 A. Equbal, S. K. Jain, Y. Li, K. Tagami, X. Wang and S. Han, *Prog. Nucl. Magn. Reson. Spectrosc.*, 2021, **126–127**, 1–16.
40 G. Menzildjian, J. Schlagnitweit, G. Casano, O. Ouari, D. Gajan and A. Lesage, *Chem. Sci.*, 2023, **14**, 6120–6148.
41 A. Venkatesh, G. Casano, Y. Rao, F. De Biasi, F. A. Perras, D. J. Kubicki, D. Siri, S. Abel, H. Karoui, M. Yulikov, O. Ouari and L. Emsley, *Angew. Chem., Int. Ed.*, 2023, e202304844.
42 D. Wisser, G. Karthikeyan, A. Lund, G. Casano, H. Karoui, M. Yulikov, G. Menzildjian, A. C. Pinon, A. Purea, F. Engelke, S. R. Chaudhari, D. Kubicki, A. J. Rossini, I. B. Moroz, D. Gajan, C. Copéret, G. Jeschke, M. Lelli, L. Emsley, A. Lesage and O. Ouari, *J. Am. Chem. Soc.*, 2018, **140**, 13340–13349.
43 S. Stoll and A. Schweiger, *J. Magn. Reson.*, 2006, **178**, 42–55.
44 S. Jannin, A. Comment and J. J. Van Der Klink, *Appl. Magn. Reson.*, 2012, **43**, 59–68.
45 A. Bornet and S. Jannin, *J. Magn. Reson.*, 2016, **264**, 13–21.

46 D. Guarin, S. Marhabaie, A. Rosso, D. Abergel, G. Bodenhausen, K. L. Ivanov and D. Kurzbach, *J. Phys. Chem. Lett.*, 2017, **8**, 5531–5536.
47 F. Jähnig, A. Himmler, G. Kwiatkowski, A. Däpp, A. Hunkeler, S. Kozerke and M. Ernst, *J. Magn. Reson.*, 2019, **303**, 91–104.
48 D. Shimon, Y. Hovav, A. Feintuch, D. Goldfarb and S. Vega, *Phys. Chem. Chem. Phys.*, 2012, **14**, 5729–5743.
49 Y. Zhao, H. El Mkami, R. I. Hunter, G. Casano, O. Ouari and G. M. Smith, *Commun. Chem.*, 2023, **6**, 1–12.
50 T. El Daraï and S. Jannin, *Chem. Phys. Rev.*, 2021, **2**, 041308.
51 W. T. Wenckebach, *Essentials of Dynamic Nuclear Polarization*, Spindrift Publications, 2016.
52 K. Kundu, M. R. Cohen, A. Feintuch, D. Goldfarb and S. Vega, *Phys. Chem. Chem. Phys.*, 2018, **21**, 478–489.
53 Y. Hovav, I. Kaminker, D. Shimon, A. Feintuch, D. Goldfarb and S. Vega, *Phys. Chem. Chem. Phys.*, 2015, **17**, 226–244.